

# Task-relevant brain dynamics among cognitive subsystems induced by regional stimulation in a whole-brain computational model

Zilu Liu,<sup>1</sup> Fang Han,<sup>2</sup> and Qingyun Wang <sup>1</sup>

<sup>1</sup>*Department of Dynamics and Control, Beihang University, Beijing 100191, China*

<sup>2</sup>*College of Information Science and Technology, Donghua University, Shanghai 200051, China*

 (Received 15 September 2022; revised 14 July 2023; accepted 11 September 2023; published 4 October 2023)

Cognition involves the global integration of distributed brain regions that are known to work cohesively as cognitive subsystems during brain functioning. Empirical evidence has suggested that spatiotemporal phase relationships between brain regions, measured as synchronization and metastability, may encode important task-relevant information. However, it remains largely unknown how phase relationships aggregate at the level of cognitive subsystems under different cognitive processing. Here, we probe this question by simulating task-relevant brain dynamics through regional stimulation of a whole-brain dynamical network model operating in the resting-state dynamical regime. The model is constructed with structurally embedded Stuart-Laudon oscillators and then fitted with human resting-state functional magnetic resonance imaging data. Based on this framework, we first demonstrate the plausibility of introducing the cognitive system partition into the modeling analysis framework by showing that the clustering of regions across functional networks is better circumscribed by the predefined partition. At the cognitive subsystem level, we focus on how task-relevant phase dynamics are organized in terms of synchronization and metastability. We found that patterns of cognitive synchronization are more task specific, whereas patterns of cognitive metastability are more consistent across different states, suggesting it may encode a more task-general property during cognitive processing, an inherent property conferred by brain organization. This consistent network architecture in cognitive metastability may be related to the distinct functional responses of realistic cognitive systems. We also provide empirical evidence to partially support our computational results. Our paper may provide insights for the mechanisms underlying task-relevant brain dynamics, and establish a model-based link between brain structure, dynamics, and cognition, a fundamental step for computationally aided brain interventions.

DOI: [10.1103/PhysRevE.108.044402](https://doi.org/10.1103/PhysRevE.108.044402)

## I. INTRODUCTION

Cognition involves a global integration of distributed brain regions [1], and deviance from such functional capacity is associated with neurological and psychological disorders [2]. Progress in brain network studies has revealed a well-structured pattern of neural activities in the human resting brain [3]. Task-evoked networks are reported to be highly correlated with the resting-state ones, and task-based functioning is assumed to be initiated by the task-specific activation of the intrinsic network architecture at rest [4]. Moreover, brain regions are found to work cohesively as grouped communities under different cognitive operations and play distinct roles in maintaining healthy brain functions [5,6]. Therefore, understanding how these patterns are dynamically formed and linked to cognitive processing is an important problem remaining to be solved.

Phase relationships among brain regions have gained increasing attention in studying macroscopic brain activities [7,8]. Phase synchronization is ubiquitous in natural systems including the brain, and conjectured to be a fundamental mechanism for neural communication [9]. Empirical and theoretical evidence has suggested that coordinated brain dynamics arise from a dynamical metastable regime that could balance functional segregation and integration [10–13].

Phase synchronization, denoted as the standard Kuramoto order parameter [14], has been demonstrated to be powerful in informing the dynamic traits of brain oscillations [15,16]. Metastability, measured as the temporal variation of the Kuramoto order parameter [12], may encode important information for cognitive processing. Empirical evidence has suggested an association between metastability and cognitive performance in both healthy cognitive operations [17] and impaired brain functions such as senescence [18] and Parkinson's disease [8]. Researchers have also speculated that a higher level of metastability is linked to higher cognitive performance, while a lower level of metastability will result in impaired cognitive performance [18]. Therefore, brain regions may rely on metastability to bind into functionally connected subnetworks during cognitive operations. However, how metastability is circumscribed by the cognitive subnetworks remains largely unclear.

Empirically, brain states can be intervened by external means such as transcranial direct current stimulation and deep brain stimulation, which have been applied to improve cognition and emotion [19] and the treatment of Parkinson's disease [20]. Effects on cognitive performance also accompany observable changes in functional connectivity patterns [19] and preferential response among specific cognitive subnetworks [20]. However, such practices are largely constrained by

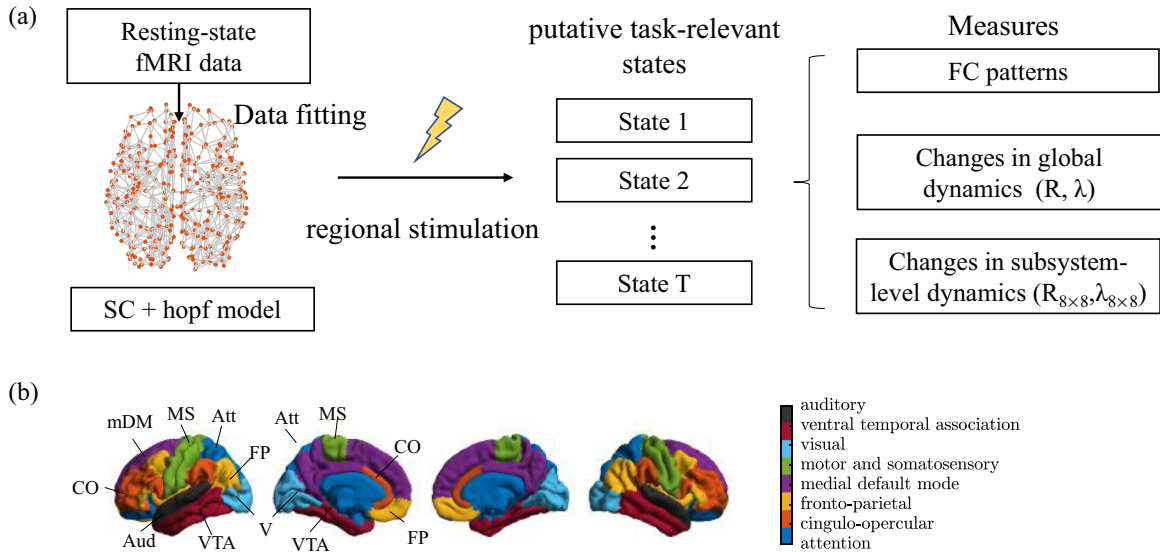


FIG. 1. (a) A schematic of modeling and analyzing methods. (b) Spatial distribution of the eight cognitive subsystems: Attention (Att), cingulo-opercular (CO), fronto-parietal (FP), medial default mode (mDM), motor and somatosensory (MS), visual (V), ventral temporal association (VTA), and auditory (Aud).

ethical restrictions that limit their capability in providing mechanistic views on the brain system. In contrast, *in silico* perturbational experiments are free of such limitations, where systematic explorations of control parameters can paint a full picture of the system's dynamic working space. Computational brain models are promising to provide mechanistic insights into the underlying link between brain structure, dynamics, and function [21]. A recently proposed modeling framework that leverages the integration of empirical neuroimaging data and theoretical neural dynamical models has been applied to approach this goal. These models have been used to elucidate the metastable nature of human resting-state networks [13,22–25]. However, dynamical insights for brain states other than rest are still lacking, especially for cognitive operations. Preliminary efforts have employed *in silico* perturbational experiments to represent task-evoked states in a general way, and measure brain synchronization among predefined cognitive subsystems [21,26]. The consistency of these patterns has been used to explain the functional roles of different cognitive subsystems [27].

We hypothesize that metastability at the level of cognitive subsystems will provide meaningful information for task-relevant operations. Task-relevant brain dynamics are generated in a phenomenological way by applying regional stimulation on a calibrated resting-state brain network model, allowing the relationship between characteristics of brain dynamics and underlying structures to be explored explicitly. We characterize both spatial and temporal aspects of brain dynamics, i.e., synchronization and metastability, at the level of predefined cognitive systems and examine their relationship to the underlying structure. We also show that the functional roles of cognitive subsystems are embodied in their metastability interactions and provide empirical evidence for this using human functional data in rest and task operations. Our results may provide a mechanistic insight into how brain functioning relies on phase relationships at the level of network communities.

## II. MODEL AND METHODS

A schematic of the simulating and analysis framework is shown in Fig. 1(a). Briefly, task-relevant brain dynamics is simulated by regional stimulation of a whole-brain dynamical network model operating in the resting-state dynamical regime. The model is composed of coupled Stuart-Laudon oscillators with human realistic structural connectivity (SC). We first demonstrate the plausibility of introducing a predefined cognitive partition into the modeling analysis framework by showing that the functional roles of systems are recovered from the simulations of putative task-relevant functional networks. The functional roles of systems are indicated by a summarized metric of common community activation called the allegiance matrix [Fig. 2(a)]. We then characterize network dynamics at the level of cognitive subsystems and examine their relationship with the underlying structure [Fig. 2(b)].

### A. Empirical data preparation

Empirical data of 20 healthy subjects were obtained from the Human Connectome Project (HCP) 100 unrelated dataset [28]. We used the minimally preprocessed structural and diffusion magnetic resonance imaging data provided by the HCP to generate group-averaged structural connectivity [29]. For each subject, a tractography of  $10 \times 10^6$  streamlines was generated under a probabilistic fiber tracking algorithm, and was further processed with spherical-deconvolution informed filtering of tracks to mitigate the bias toward overestimating long tracks. We parcellate the brain into  $N = 68$  cortical regions using the Desikan-Killiany atlas [30]. Then the structural connectivity matrix  $C$  was generated by counting the number of streamlines between pairwise regions, and normalized by the region's volume. To compute the group SC, each individual SC was thresholded to exclude potential false positives if connections of the pairwise regions were zero in more than half of the subjects [31].

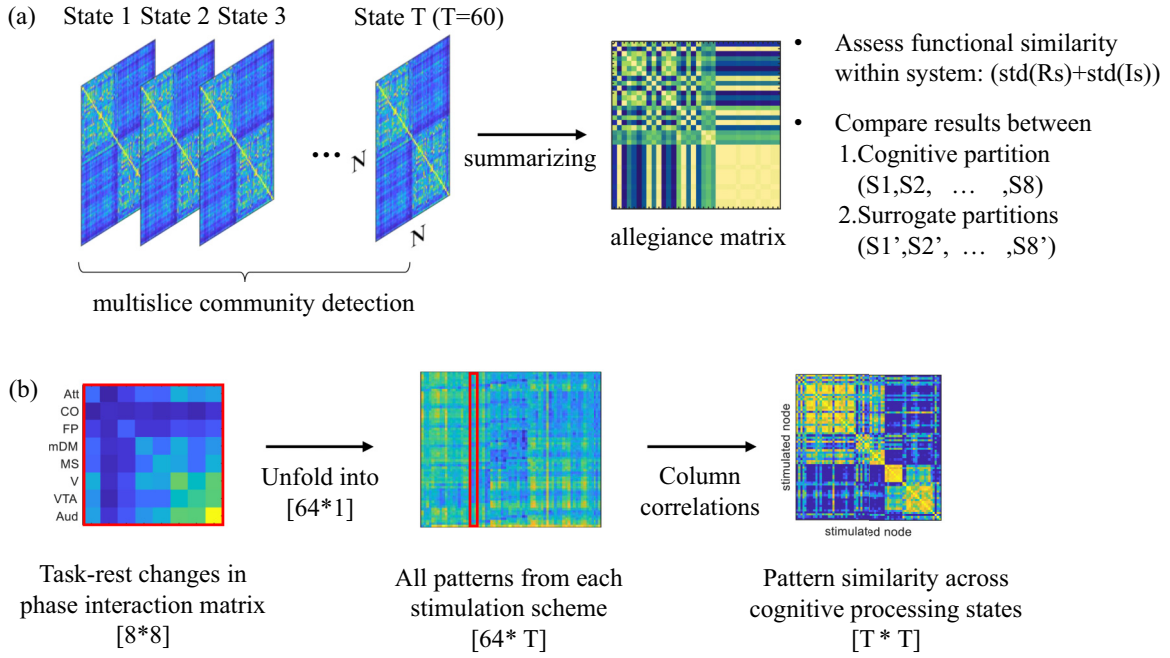


FIG. 2. A schematic of analysis methods for the results. (a) Procedure of obtaining module allegiance across brain states to demonstrate the clustering of regions within predefined cognitive subsystems. (b) Visualization of the similarity between cognitive synchronization metastability patterns across task-relevant states under specific stimulation schemes.

Time series of preprocessed resting-state blood oxygen level dependent (BOLD) signals were extracted at the voxel level (repetition time = 0.72 s, 14.4 min) and then averaged within the same regions defined by the Desikan-Killiany atlas ( $N = 68$ ) for each subject and each session (four sessions in total). The signals were filtered in a narrowband of 0.04–0.07 Hz that is thought to be most functionally relevant with resting-state dynamics [15,16].

### B. Whole-brain dynamical network model

The whole-brain computational model is based on anatomically constrained coupled nonlinear oscillators. Despite its phenomenological nature compared to biophysically realistic models, theoretical studies have shown its capability of explaining brain dynamics in the resting state [12,32].

Dynamics of each brain region  $i$  were generated by the Stuart-Landau oscillator [33], also known as the Hopf model denoting the normal form of supercritical Hopf bifurcation. The Hopf model is capable of describing the dynamical transition between noise and oscillation, has been demonstrated to exhibit the richness and generality of observed EEG signals at the local level, and is thus frequently employed as a representative of mesoscopic neural dynamics [34,35]:

$$\frac{dx_i}{dt} = (a_i - x_i^2 - y_i^2)x_i - \omega_i y_i + \beta \eta_i(t), \quad (1)$$

$$\frac{dy_i}{dt} = (a_i - x_i^2 - y_i^2)y_i + \omega_i x_i + \beta \eta_i(t) \quad (2)$$

where  $a_i$  is the bifurcation parameter with a critical value of zero. State variables  $x_i$  and  $y_i$  describe the node dynamics in Cartesian coordinates, and we take  $x_i$  as a phenomenological representation of the regional BOLD signal. The intrinsic

frequency  $f_i = 2\pi/\omega_i$  is set equal to the peak frequency of the corresponding functional magnetic resonance imaging (fMRI) time series in the range of 0.04–0.07 Hz reported to be most functionally relevant.  $\eta_i(t)$  is the Gaussian noise with a strength of  $\beta = 0.002$ .

Hopf oscillators are coupled through the structural connectivity matrix  $C$  that was derived from human structural data. The full model is described as follows:

$$\frac{dx_i}{dt} = (a_i - x_i^2 - y_i^2)x_i - \omega_i y_i + k \sum_{j=1}^N C_{ij}(x_j - x_i) + \beta \eta_i(t), \quad (3)$$

$$\frac{dy_i}{dt} = (a_i - x_i^2 - y_i^2)y_i + \omega_i x_i + k \sum_{j=1}^N C_{ij}(y_j - y_i) + \beta \eta_i(t) \quad (4)$$

where  $i, j = 1, 2, \dots, N$  indexes various cortical regions. Diffusive coupling is used as the simplest approximation of the general coupling function and is valid in the weakly coupled oscillator limit [25].  $C$  was normalized such that its maximal entry equals 0.2 to scale range of a grid search in the parameter space.  $k$  is a scaling factor representing the global coupling strength between all the brain regions.  $a_i$  is set to be the same among all the regions and tuned together with  $k$  to find candidate working points for resting-state dynamics.

Simulation under each parameter set was run for 16.4 min with a step of  $dt = 0.001$  s and random initial conditions, and the first 2 min of activities were discarded as transients. Simulation under each parameter set was repeated 150 times, over which the dynamical measures were averaged to achieve convergent values.

### C. Measures of functional connectivity and phase dynamics

Functional connectivity (FC) was obtained by computing the Pearson correlation of the fisher  $z$ -transformed pairwise time series as a time-averaged measure of coherence for both empirical and simulated signals. The empirical group-level FC was obtained by averaging across all the subjects and sessions. The temporal dynamics of FC is represented by the functional connectivity dynamics (FCD) to provide information of network coherence in temporal aspects [24,25]. FCD is obtained first by truncating the time series with a sliding window approach (window length = 60 s, overlap = 59 s), and a static FC matrix was calculated for each window resulting in a series of  $C_{\text{func}}(t)$ . Then, the FCD matrix is defined by the pairwise correlation between all the possible  $C_{\text{func}}(t)$  pairs, where transient stable FC states would appear in the matrix as squared patterns.

Phase synchronization is measured by the Kuramoto order parameter [14], which is given by

$$R(t) = \left| \frac{1}{N} \sum_{j=1}^N \exp[i\phi_j(t)] \right| \quad (5)$$

where  $\phi_j$  is the instantaneous phase of the  $j$ th region at time  $t$ . The instantaneous phase is obtained by applying the Hilbert transform to the narrowband signal  $x(t)$ :

$$z(t) = x(t) + iH[x(t)] \quad (6)$$

where  $i$  is the imaginary unit, and  $H$  denotes the Hilbert transformation. The variable  $z(t)$  is a complex signal whose argument and modulus denote the phase and the amplitude of the narrowband signal, respectively.

The global synchronization is obtained by averaging  $R(t)$  over the whole time course ( $t_{\text{total}}$ ), and metastability is measured as the fluctuation of  $R(t)$  to indicate the temporal aspects of brain dynamics:

$$\lambda = \frac{1}{\lambda_{\text{max}}} \left\{ \frac{1}{t_{\text{total}} - 1} \sum_{t \leq t_{\text{total}}} [R(t) - \langle R(t) \rangle_{t_{\text{total}}}]^2 \right\}. \quad (7)$$

Here,  $\lambda_{\text{max}} = \frac{1}{12}$  is a normalization factor representing the scenario with maximal metastability [10]. For empirical values, the global synchronization and metastability were averaged across all the subjects and sessions to represent the group-level dynamics.

In this paper, we put a special focus on network dynamics at the level of the well-defined cognitive subsystems. Since the instantaneous phase is computed for each region separately, the interactive phase relationship among subsystems can be quantified by computing Kuramoto order parameters among regions from pairwise subsystems in a network format, leading to cognitive synchronization and metastability. The two measures are defined as follows:

$$R_{S_i, S_j}(t) = \left| \frac{1}{N_{S_i} + N_{S_j}} \sum_{j \in S_i, S_j} \exp[i\phi_j(t)] \right|, \quad (8)$$

$$R_{S_i, S_j} = \langle R_{S_i, S_j}(t) \rangle_{t_{\text{total}}}, \quad (9)$$

$$\lambda_{S_i, S_j} = \frac{1}{\lambda_{\text{max}}} \left\{ \frac{1}{t_{\text{total}} - 1} \sum_{t \leq t_{\text{total}}} [R_{S_i, S_j}(t) - \langle R_{S_i, S_j}(t) \rangle_{t_{\text{total}}}]^2 \right\}. \quad (10)$$

Here,  $S_i$  means region  $i$  is a member of the subsystem  $S$ . The 68 regions were allocated into eight subsystems following Ref. [27] [see Fig. 1(b)], which are the attention (Att), cingulo-opercular (CO), fronto-parietal (FP), medial default mode (mDM), motor and somatosensory (MS), visual (V), ventral temporal association (VTA), and auditory (Aud) system.

### D. Fitting the model with empirical resting-state fMRI data

A typical workflow of the brain network modeling framework is to constrain model behavior with metrics derived from empirical functional data [36]. To obtain a model operating in the resting state, we fit the model to empirical data based on four metrics: Static FC, FCD, global synchronization, and metastability. FC and FCD characterize network synchronization from the amplitude perspective; the former is a statistical average over time and focuses on the spatial aspect, and the latter is the summary of FCs in consecutive time windows and focuses on the temporal aspect. It was suggested that fitting FCD could reflect the dynamic switching of FC states which cannot be obtained by fitting grand-average FC only [25]. The Kuramoto order parameter characterizes network synchronization from the phase coherence perspective. Empirical evidence has suggested that global phase synchronization is a sensitive metric in differentiating two brain states [16], and global metastability was found to be maximal in the model's best fitting regime [25]. We take these considerations in all to determine the model's best working point to reproduce resting-state dynamics.

We evaluate model performance by measuring the difference between empirical and simulated values. The similarity between empirical and simulated FCs is measured as the Pearson correlation between the upper triangular entries of the two matrices ( $C_{\text{func. corr.}}$ ). The Kolmogorov-Smirnov distance ( $d_{\text{KS}}$ ) is used to compare the cumulative sum of the upper triangular entries of the FCD matrices. Global dynamics are measured by the absolute difference between the empirical and the simulated values ( $d_{\text{R}}$  and  $d_{\lambda}$ ). We expect  $C_{\text{func. corr.}}$  to be close to 1, and we expect  $d_{\text{KS}}$ ,  $d_{\text{R}}$ , and  $d_{\lambda}$  to be close to zero. Thereby we use an integrated metric to summarize all these effects like in Ref. [37]. The four metrics were integrated as

$$D = (1 - C_{\text{func. corr.}})d_{\text{KS}}d_{\text{R}}d_{\lambda}. \quad (11)$$

A smaller  $D$  indicates a better model performance, and the best-fitted parameter set [ $a_{\text{best}}$ ,  $k_{\text{best}}$ ] is identified when  $D$  achieves its minimum.

### E. Modeling putative task-relevant states by regional stimulation

By considering the brain as a dynamical system, it is suggested that spontaneous brain dynamics in the resting state carry information about how the brain explore the dynamics repository of all possible functional states [13]. Task-evoked

networks are reported to be highly correlated with the resting-state ones, and task-based functioning is assumed to be initiated by the task-specific activation of the intrinsic network architecture at rest [4]. We hypothesize that stimulation involving different brain regions would encode particular cognitive processing. In this paper, task-relevant brain dynamics are simulated by applying regional stimulation to the fitted resting-state dynamical model in a phenomenological way. The effect of stimulation was modeled by changing the value of the bifurcation parameter  $a_i$  of the stimulated regions  $i$  into  $a_s$ . The perturbation is chosen mainly based on phenomenological considerations. As the Hopf model is a phenomenological representation of regional dynamics, the local bifurcation parameter  $a_i$  does not have a direct biological correlate with real systems. But in a dynamical sense, it defines the distance to a supercritical Hopf bifurcation which can exert a significant impact on local dynamics, and its change can be related to some general effects of biological processes in an abstract way. We performed four stimulation schemes by considering the direction of perturbations and the numbers of stimulated regions being single or multiple (ten randomly selected regions), which are denoted as single stimuli (+), single stimuli (-), multiple stimuli (+), and multiple stimuli (-) (with  $a_s = [0.1, -1, 0.01, -0.4]$ , respectively). The positive (negative) values of  $a_s$  aim to drive the model with a qualitative dynamic consequence of moving closer to (away from) the oscillatory regime relative to  $a_{\text{best}}$  at rest.

#### F. Evaluating the clustering of simulated task-relevant brain activities

We evaluate whether the simulated brain states could recover the clustering of brain regions under empirical cognitive processing [5]. The common community architecture across activated states is first detected by the Louvain algorithm and then summarized by the allegiance matrix. Each entry of the allegiance matrix indicates the probability of coactivation for pairwise regions across different task operations which allows us to characterize the functional roles of the cognitive subsystems using its derived coefficients. A schematic of the analysis procedure is given by Fig. 2(a).

More in detail, under a specific stimulation scheme, a set of FCs from  $T = 60$  stimulation-induce task-relevant states is generated, and then we apply a generalized Louvain algorithm to obtain a consistent community detection across multiple networks [38,39]. Briefly, multiple FC matrices were treated as a multislice system linked by interslice connections, and a categorical multislice Louvain detection was performed to obtain a consistent community partition that maximizes the modularity  $Q$ , which is defined as

$$Q(\gamma, \omega) = \frac{1}{l} \sum_{ijsr} \left[ \left( a_{ijs} - \gamma_s \frac{k_i k_j}{l} \right) \delta(\sigma_{is}, \sigma_{js}) + \delta(i, j) \omega_{jrs} \right] \times \delta(\sigma_{is}, \sigma_{jr}) \quad (12)$$

where  $l$  represents the sum of all weights in the network, and  $k_i$  is the degree of node  $i$ .  $a_{ijs}$  denotes the connectivity of the multislice network with subscript  $s$  indexing slices.  $\delta(i, j) \omega_{jrs}$  is the coupling strength between slice  $s$  and  $r$ .  $\delta$  is the Kronecker delta function and equals to 1 if the community

assignments  $\sigma$  are the same.  $\gamma$  and  $\omega$  are resolution parameters to control the size and number of detected communities ( $M$ ). We explored various combinations of parameters in the range of  $\gamma \in [0.5, 1.2]$  and  $\omega \in [0.3, 0.8]$  with a step size of 0.05. Then a specific parameter regime is identified to allow meaningful difference between resting and task-relevant states, so that resting and task FCs have equivalent number of communities with  $M \geq 3$ . This choice is to avoid overly coarse partitions involving the whole left or right hemisphere.

The obtained community structures with a size of  $[N, T, O]$  are summarized into  $[N, N]$  using a metric called the allegiance matrix  $P$  [5,40]:

$$P_{ij} = \frac{1}{OT} \sum_{o=1}^O \sum_{t=1}^T u_{i,j}^{t,o} \quad (13)$$

where  $O$  is the number of runs of the algorithm ( $O = 100$ ), and  $T$  is the number of task slices ( $T = 60$ ).  $u_{i,j}^{t,o}$  equals 1 if nodes  $i$  and  $j$  are assigned into the same community and zero otherwise.

The allegiance matrix gives a picture about how regions are functionally connected across task operations. Assuming that regions are clustered into different cognitive subsystems, we use two metrics derived from the allegiance matrix directly, namely, network recruitment  $R_i^S$  and integration  $I_i^S$ , to quantify the functional role of each region  $i$  with respect to a specific cognitive subsystem  $S$ :

$$R_i^S = \frac{1}{n_S} \sum_{j \in S} P_{ij}, \quad (14)$$

$$I_i^S = \frac{1}{N - n_S} \sum_{j \notin S} P_{ij} \quad (15)$$

where  $n_S$  is the total number of regions in system  $S$ , and  $N$  denotes the total number of regions in the network. Briefly, recruitment and integration measure the tendency of a given region to be activated together with regions from the same or other system(s). To evaluate how critical the predefined cognitive system partition is to circumscribe functional activities, we quantify the similarity of functional roles for regions within a particular system. Functional similarity is calculated simply as the sum of standard deviations of recruitment and integration, which is given by  $\text{std}(R^S) + \text{std}(I^S)$ .

To give more intuition for the above methods, a schematic is given in Fig. 2.

### III. RESULTS

#### A. Resting-state dynamics simulated by fitting the whole-brain dynamical model with empirical fMRI data

We commence by fitting the model to human realistic resting-state fMRI data. In this paper, four metrics are used to constrain the model's behavior, including FC, FCD, global synchronization, and metastability, and their distance to the corresponding empirical value is measured as  $C_{\text{func. corr.}}$ ,  $d_{\text{KS}}$ ,  $d_{\text{R}}$ , and  $d_{\lambda}$ .

We explored the combination of bifurcation parameter  $a$  and global coupling strength  $k$  to evaluate the performance of simulated activities. Consistent with previous work that employed a similar modeling framework [16,41], the

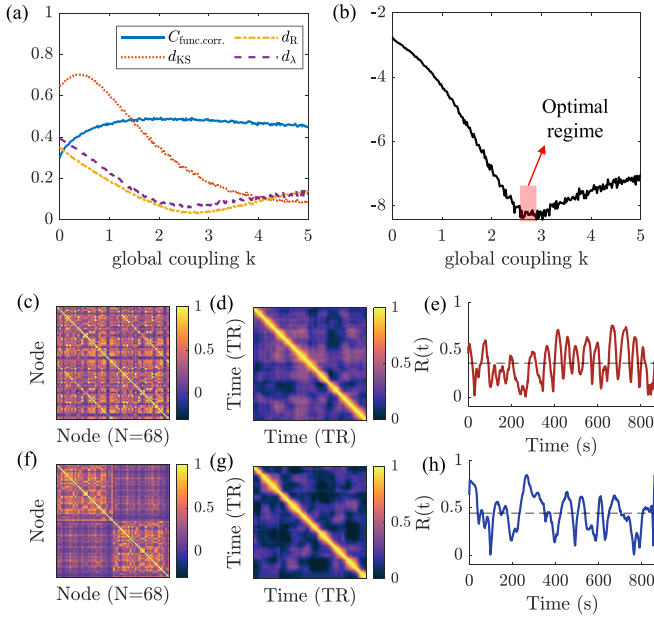


FIG. 3. Model fitting with empirical resting-state fMRI data. (a) The fitting curve of  $C_{\text{func.corr.}}$ ,  $d_{\text{KS}}$ ,  $d_{\text{R}}$ , and  $d_{\lambda}$ , respectively, as a function of global coupling  $k$  with  $a = -0.04$ . (b) The curve of the integrated metric  $D$ , with the optimal regime indicated by the shaded area. Simulated network dynamics at the chosen working point ( $a = -0.04$ ,  $k = 2.72$ ) are given by (c) FC, (d) FCD, and (e) time-varying Kuramoto order parameter, with its mean and standard deviation denoting synchronization and metastability, respectively. (f–h) The same metrics computed from empirical fMRI data.

best-fitting regime lies within  $-0.04 \leq a \leq -0.06$ , and  $k > 0.5$ . The fitting of each metric as a function of  $k$  when  $a = -0.04$  is given by Fig. 3(a). It can be seen that the metrics vary distinctly with respect to  $k$ , with  $C_{\text{func.corr.}}$  expected to be 1 and others expected to be zero. In order to summarize the overall fitting performance, an integrated metric  $D$  is used. Figure 3(b) shows the performance curve of  $D$ , where the red shaded area indicates the best-fitting regime with minimum  $D$ . We chose a specific parameter set  $a = -0.04$ ,  $k = 2.72$  from the best-fitting regime as a representative working point of the simulated resting state. Dynamics of the model at the working point are displayed in Figs. 3(c)–3(e), as compared with those of empirical data [Figs. 3(f)–3(h)].

### B. Clustering of simulated task-relevant brain activities within the predefined cognitive subsystems

Task-relevant brain activities are simulated by applying regional stimulation to the fitted resting-state model. Such a practice is inspired by the empirically proposed hypothesis that task-based brain functioning is initiated by the activation of intrinsic network architecture at rest [4]. Each task-relevant brain state is induced via adjusting the bifurcation parameter  $a_i$  from  $a_{\text{best}}$  to  $a_s$  in one node or multiple nodes at a time (details in Sec. II E). Empirical evidence suggests that brain regions tend to work cohesively as communities during task operations [5]. In order to evaluate whether the simulated activities could recover such a feature, and to provide reasonable evidence for analyzing dynamics subsequently at the cognitive

system level, we examine the common community structure across activated FCs and its accordance with the predefined cognitive system partition.

We obtained consistent network modules for all the 60 activated FCs using the Louvain algorithm [38]. The degree of network modularity is measured by the number of communities  $M$  and modularity  $Q$ . Their difference with the resting-state value is displayed on the space of  $[\omega, \gamma]$  which are the control parameters of the Louvain algorithm. Figure 4(e) shows that the modularity of task-operating networks is always lower than the resting ones over the whole parameter space, which is in line with empirical findings of functional networks [42]. We obtain meaningful community detections in the parameter range within the marked rectangle in Fig. 4(f), where resting and task FCs have equivalent number of communities with  $M \geq 3$ . This choice is to avoid overly coarse partitions involving the whole left or right hemisphere.

Based on the obtained communities at  $\gamma = 1$  and  $\omega = 0.5$ , we employ an empirically proposed metric, the allegiance matrix [5,40], to assess the probability of pairwise regions to be coactivated across states. The result is illustrated in Fig. 4(a), and the regions are rearranged in the order of eight cognitive subsystems as in Fig. 1(b). It is revealed that regions from some subsystems have qualitatively distinguished module allegiance properties from others (such as CO vs V), and generally accord with the boundary of the predefined eight systems. To give a full picture of how the cognitive subsystems are functionally activated, we characterize the functional role of each subsystem using the derived metrics of the allegiance matrix. Briefly, recruitment and integration measure the tendency of a given region to be activated together with regions from the same system, or from systems other than itself. It can be seen from Fig. 4(c) that systems like MS, V, VTA, and Aud are highly self-recruited, while CO and FP tend to integrate with other systems with lower recruitment [Fig. 4(d)]. This divergence of system function generally agrees with the partition between primary sensory and higher cognitive systems. Note that the simulations are interpreted qualitatively because of the poor representation of cross-hemisphere connections.

To demonstrate that such system function is not observed by chance and critical to the predefined system partition, we evaluated the functional role of the system under surrogate partitions. Functional similarity of regions from the same system is quantified by the standard deviation of integration and recruitment:  $\text{std}(R^S) + \text{std}(I^S)$  as marked by the blue crosses in Fig. 4(b). This value is expected to be small enough, indicating that regions within a system share similar functional roles. Surrogate values are computed under randomized partitions to interpret the degree of such similarity. Surrogate partitions were generated by randomly grouping network nodes into eight systems, with each system preserving the same number of regions as in the cognitive partition. We ran 500 realizations of surrogate system partitions and obtained the distributions of functional similarity as the boxplots in Fig. 4(b).

It is shown that functional similarity within the primary sensory systems (i.e., MS, V, VTA, Aud) is highly differed from the surrogate distributions and closer to the zero axis. This indicates that these systems have regions sharing more similar functional roles only if grouped by the predefined sub-

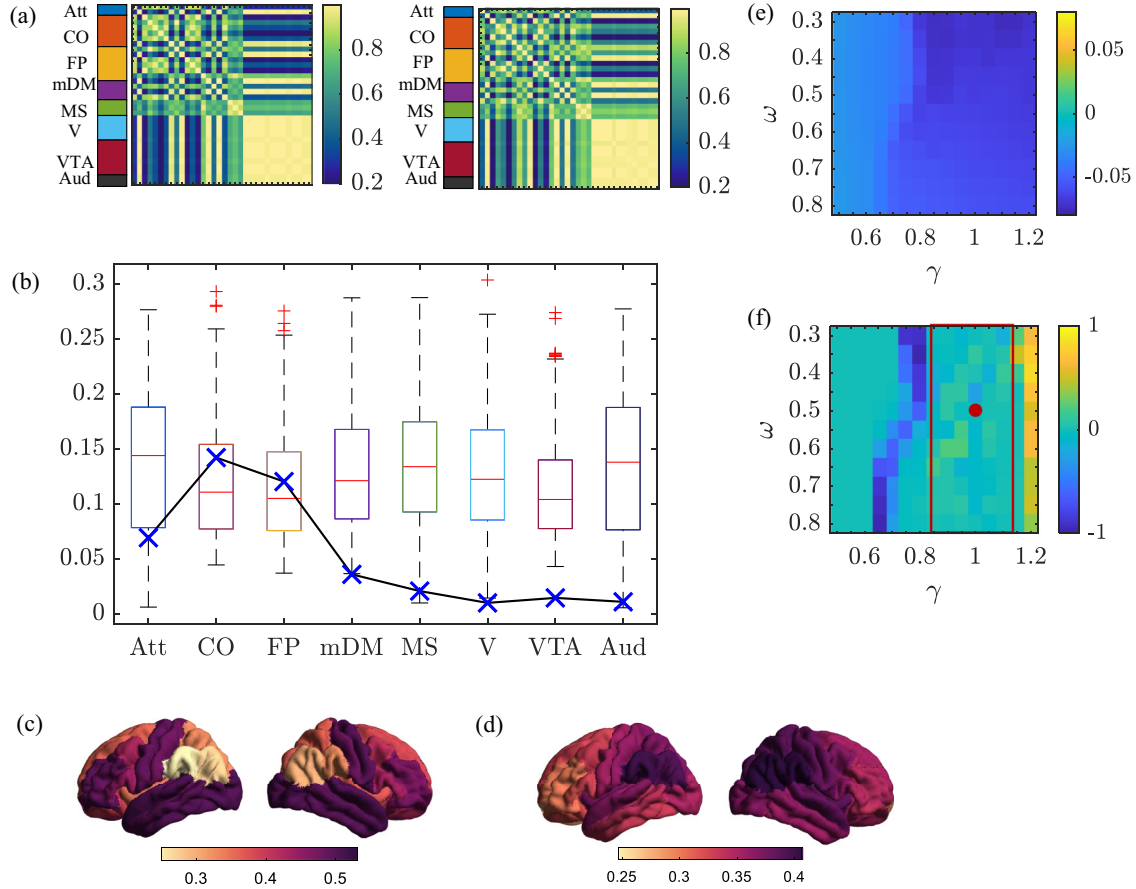


FIG. 4. The clustering of brain regions across stimulation-induced brain networks. (a) Allegiance matrix of the left (left panel) and right (right panel) hemisphere that measures the probability of coactivation for pairwise regions across states. (b) Functional similarity [measured as the sum of the standard deviation of integration and recruitment,  $\text{std}(R^S) + \text{std}(I^S)$ ] of nodes under the cognitive partition (marked by blue crosses) and surrogate partitions (box distributions). (c, d) The spatial distribution of (c) recruitment ( $R_i^S$ ) and (d) integration ( $I_i^S$ ) derived from the allegiance matrix in (a). (e, f) The difference in (e) the numbers of communities ( $M_{\text{task}} - M_{\text{rest}}$ ) and (f) the value of modularity ( $Q_{\text{task}} - Q_{\text{rest}}$ ) as results of the Louvain algorithm on the plane of  $[\omega, \gamma]$ .

systems. Though the phenomenon may partly be contributed by the underlying highly connected structural links (such as within the visual system), we notice that there are cognitive systems, e.g., the motor and somatosensory system, that were identified by the allegiance matrix while they cannot be aggregated as a well-defined structural module (i.e., regions belonging to MS are assigned into three different structural modules by applying the Louvain algorithm to the SC matrix). Therefore, the observed within-system functional similarity in MS is not as straightforward as what can be expected from the underlying SC directly. We also observed that the functional similarity within CO and FP cannot be distinguished from the surrogate values. In addition to limitations in the model paradigm itself, this may also reflect the function of cognitive control systems (Att, CO, FP) to be more diverse within themselves across task operations.

### C. Task-relevant changes in global synchronization and metastability

Global phase dynamics are suggested as a potential neural communication mechanism underlying cognitive performance, and their alterations are reported in Parkinson's and Alzheimer's disease [8,43,44]. We first examine how global

dynamics changes during task operations and the contribution of local structural property. Compared to the resting-state value, global synchronization and metastability change significantly ( $p < 0.01$ ) after stimulation, as shown in Figs. 5(a) and 5(b). Generally, positive (+) schemes will induce an increase in both synchronization and metastability, and negative schemes are opposite. We excluded the patterns from the fully coherent regime, which are considered not relevant in the task-relevant scenario. For single stimuli schemes, we also investigate the relationship between changes in global dynamics and SC strength, which is defined as the summed connection weights of each node in SC. As revealed by Figs. 5(c) and 5(e), changes in global synchronization show a negative correlation with the SC strength of the stimulated node ( $r = -0.59$ ,  $p \leq 0.01$ ;  $r = -0.40$ ,  $p \leq 0.01$ ) under both positive and negative schemes, while metastability is predictable under the positive scheme only ( $r = -0.59$ ,  $p \leq 0.01$ ;  $r = -0.18$ ,  $p = 0.1$ ) [Figs. 5(d) and 5(f)]. We did not observe a spatial preference between the stimulated cognitive system and changes in global dynamics. Such results suggest the simulated global dynamics cannot reflect the functional role of cognitive systems, and are largely constrained by the underlying structural connectivity.

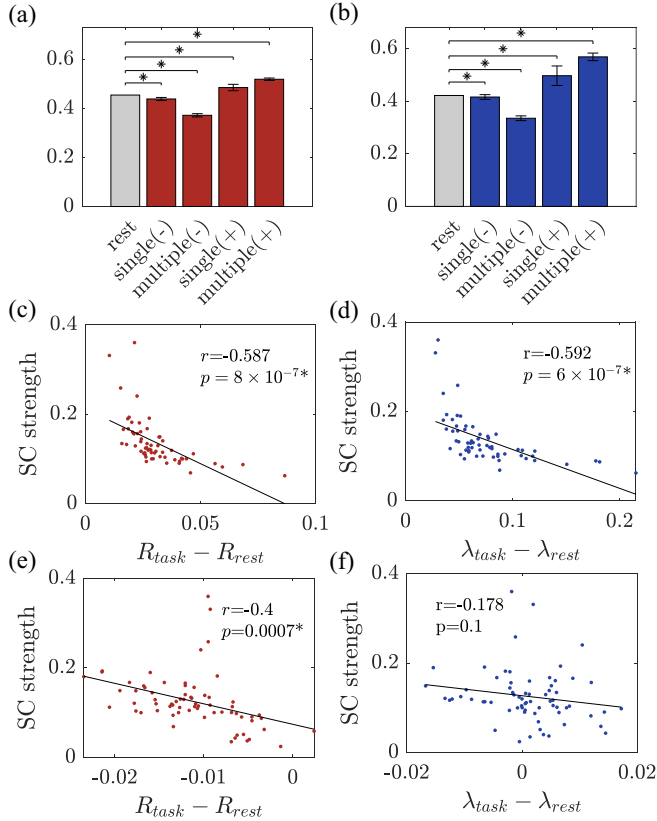


FIG. 5. Stimulation-induced changes in global network dynamics and contribution of structural connectivity. (a, b) Statistics of (a) global synchronization and (b) metastability at rest and after stimulation. The error bar indicates the standard deviation across all 60 states under each scheme. (c–f) Correlations between SC strength and changes in global synchronization for the (c) single stimuli (+) and (e) single stimuli (–) scheme, and in global metastability for the (d) single stimuli (+) and (f) single stimuli (–) scheme.

#### D. Task-relevant changes in cognitive synchronization and metastability networks

Assuming that system-level analysis of phase dynamics may provide valuable insights related to cognitive processing, we compute cognitive synchronization and metastability networks and obtain the difference between task-relevant and resting-state patterns. Similarities of cognitive synchronization and metastability networks across stimulation-induced states are displayed in Figs. 6(a) and 6(b). For single stimuli schemes, the similarity matrix is ordered by the results of stimulating each system sequentially [from Att to Aud as shown in Fig. 1(b)], whereas for the multiple stimuli schemes the order refers to the random 60 realizations of stimulation experiments. It is shown that under single stimuli schemes the similarity matrices are highly modularized with boundaries accordant with the predefined cognitive systems, which means stimulating regions from the same system would result in more similar changes in dynamical patterns [the left two panels in Fig. 6(a)]. Under multiple stimuli schemes, though the overall level of pattern similarity is much higher, it is still diverse between states [the right two panels in Fig. 6(a)]. In contrast, the changes in cognitive metastable networks are

much more similar across states, with the similarity matrices having entries close to 1 [Fig. 6(b)], which means a relatively consistent pattern is obtained from stimulating different regions. It can be thus summarized that changes in cognitive synchronization networks are more sensitive to where the stimuli are applied, while those in cognitive metastability networks are relatively consistent across task operations. Since each stimuli implementation encodes a potential cognitive processing under task paradigms, these results suggest that cognitive synchronization patterns may be task specific, while the cognitive metastable networks may reflect a general architecture across states.

#### E. Functional role of cognitive systems embodied in the architecture of cognitive metastable networks

We have found that cognitive metastability has a relatively consistent network architecture across states, but it is not clear whether it can be linked to the known functional roles of cognitive subsystems. We first display this consistent architecture in Figs. 7(a) and 7(b), and each network is obtained by averaging the cognitive metastable networks over all the 60 states. It can be seen that the general structure of the cognitive metastable network is similar for the same direction of dynamical perturbation. We also observed that the metastability changes among cognitive control and association systems (Att, CO, FP, VTA) and primary sensory systems (mDM, MS, V, Aud) are in the opposite direction for positive and negative stimulation schemes [Fig. 7(a1), above and below the dashed line].

The functional role of each system embodied in the architecture of the cognitive metastable network is portrayed in terms of its network statistics. The total amount of metastable interactions within and between each system is denoted as within metastability  $\lambda_{S_i, S_i}$  and between metastability  $\sum_{j \neq i} \lambda_{S_i, S_j}$ , and the resulting functional role of a system is reflected by its position on the plane of the two metrics [Figs. 8(a) and 8(b)]. Under the positive schemes, between metastability increases for all systems [Figs. 8(a1) and 8(a2)] while it mostly decreases under the negative schemes [Figs. 8(b1) and 8(b2)]. We observed that the functional roles of the system can be roughly divided in terms of the cognitive control and association systems and the primary sensory systems as well. Within and between metastability in cognitive control and association systems (Att, CO, FP, VTA) generally increase (or decrease) more than the default mode and primary sensory systems (mDM, MS, V, Aud) under the positive (or negative) schemes, showing that they tend to react more flexibly to incoming stimuli. This is consistent with empirical knowledge, such as the attentional system showing greater variability in functional roles than the default mode, visual, and somatosensory systems across tasks [5], and also between subjects [45].

A great advantage of investigating phase relationships between brain signals is that it allows a direct comparison between theoretical and empirical results. We empirically provide evidential support for the computational results. We used fMRI data from 98 HCP participants for resting and seven tasks (including emotion perception, gambling, language processing, motor responses, relational reasoning, social cog-

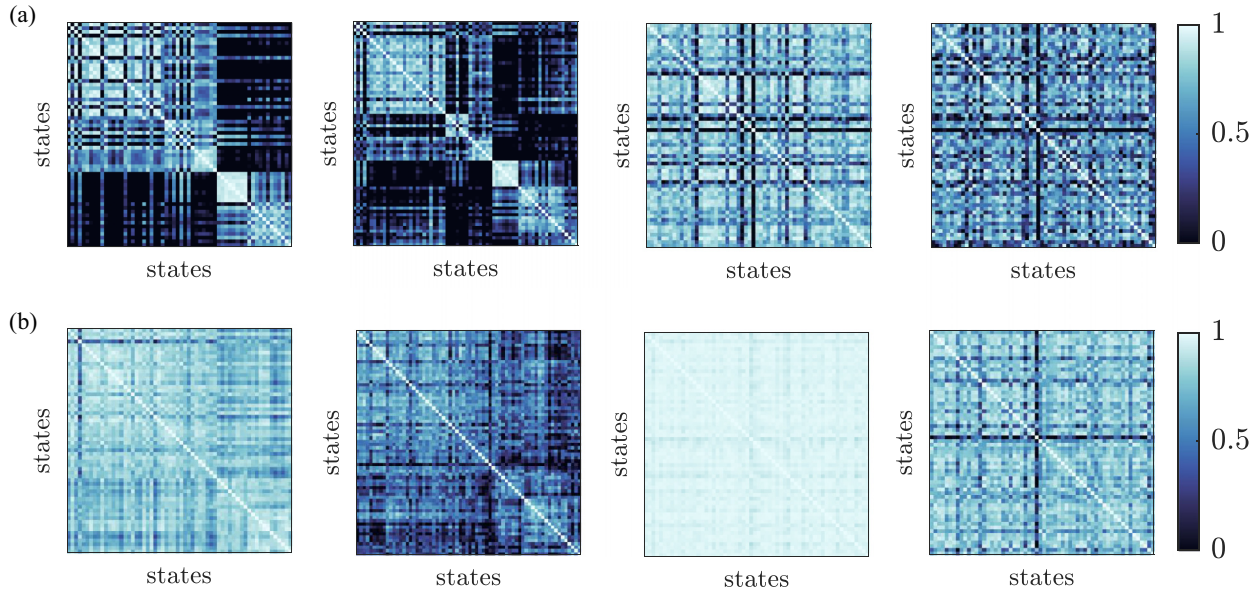


FIG. 6. Similarity between changes in cognitive (a) synchronization and (b) metastability patterns across states. For single-region stimulation schemes, the similarity matrix is ordered by the results of stimulating each system sequentially [from Att to Aud as shown in Fig. 1(b)], whereas for the multiple stimuli schemes, the order refers to the random 60 realizations of stimulation experiments. The similarity matrix of metastability has entries closer to 1 than the corresponding matrix for synchronization.

tion, and working memory), where each task contained two sessions with different lengths while the total duration of the seven tasks was 1 h. The data were processed in the same way as mentioned above. For each subject and each task, we obtained the cognitive metastable network as the task-to-rest difference between cognitive metastability patterns.

Figure 9 shows the empirical cognitive metastable network under each task, and only the interactions with statistically significant changes ( $p < 0.01$ ) are plotted as group

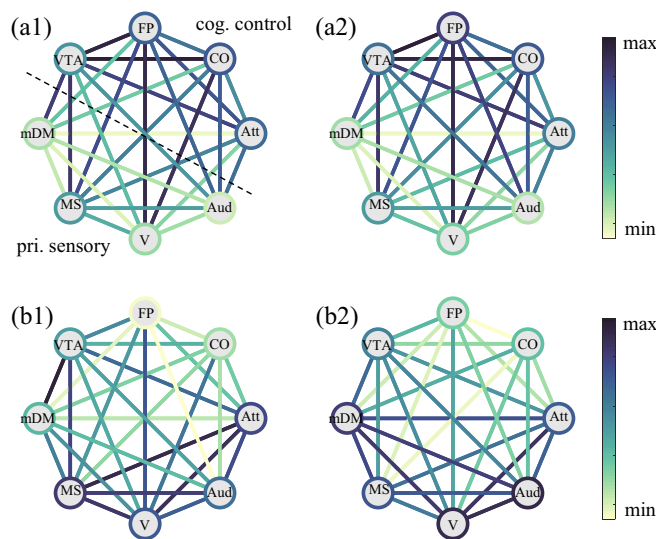


FIG. 7. The average cognitive metastable networks under the four stimulation schemes, with strength of metastability interactions encoded by the color of connections: (a1, a2) positive (+) stimuli and multiple schemes and (b1, b2) negative (-) single and multiple stimuli schemes.

averages. Overall, the cognitive control systems (Att, CO, FP, VTA) tend to have increased metastability interactions, while the primary sensory systems (mDM, MS, V, Aud) tend to have decreased metastability interactions. The darkest connections are around CO and FP, while the most

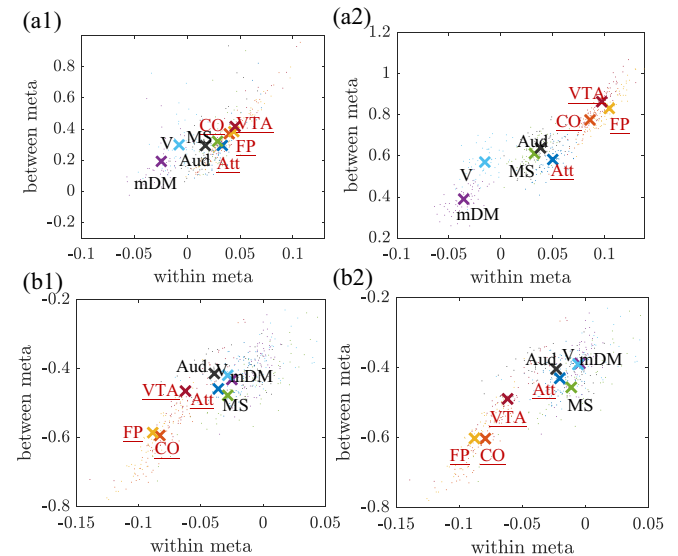


FIG. 8. The functional roles of systems embodied in the architecture of cognitive metastable networks. Functional roles of subsystems are indicated on the plane of within and between metastability. Dots denote the role for each state and crosses denote the average over all states. Labels of cognitive control and association systems (Att, CO, FP, VTA) are marked with red color and underlines to differentiate from primary sensory systems (mDM, MS, V, Aud): (a1, a2) positive (+) stimuli and multiple schemes and (b1, b2) negative (-) single and multiple stimuli schemes.

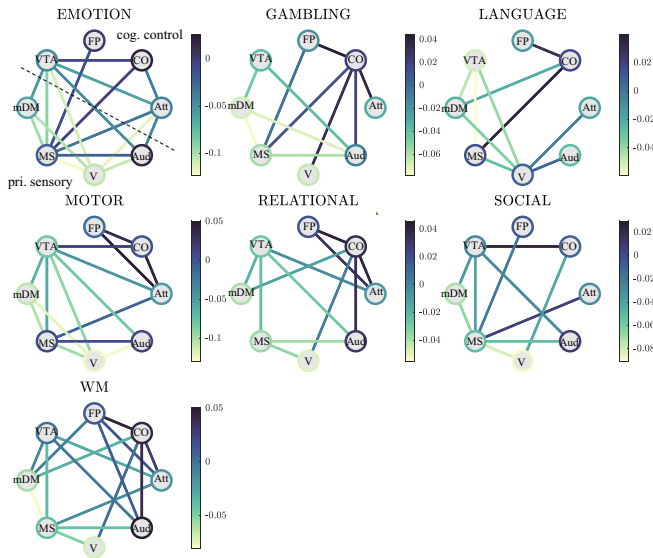


FIG. 9. Empirical cognitive metastable networks derived from HCP resting and task data. We used fMRI data from 98 HCP participants for resting and seven tasks (including emotion perception, gambling, language processing, motor responses, relational reasoning, social cognition, and working memory). The networks are displayed in the same fashion as Fig. 7, while only the interactions with statistically significant changes ( $p < 0.01$ ) are plotted as group averages.

decreased ones are around mDm and V, which is consistent with the computational results under the positive stimulation scheme [Fig. 7(a)]. Although this result was derived from only a limited number of tasks and subjects, it can qualitatively support that cognitive metastable networks exhibit similar patterns across task operations and have distinct functional responses between cognitive control systems and primary sensory systems.

IV. CONCLUSION AND DISCUSSION

In this paper, we focused on how task-relevant brain phase dynamics are organized at the level of cognitive subsystems. Task-relevant dynamics are generated in a phenomenological way by applying regional stimulation on a calibrated resting-state brain network model, allowing the relationship between characteristics of brain dynamics and underlying structures to be explored explicitly. We first demonstrated the plausibility of introducing the cognitive system partition into the modeling analysis framework. Second, we found that patterns of cognitive synchronization are more task specific, whereas patterns of cognitive metastability are more consistent across different states. Third, this consistent architecture of cognitive metastable networks can reflect the distinct functional responses between cognitive control systems and primary sensory systems. We also provided empirical evidence to partially support our computational results. These results may provide a mechanistic insight into how brain functioning relies on phase relationships at the level of network communities, thereby establishing a model-based link between brain structure, dynamics, and cognition, which is a fundamental step for computationally aided brain interventions.

The contribution of this paper is twofold. First, we demonstrate the biological plausibility of introducing the cognitive system partition into modeling analysis. The common community structure across a set of stimulation-induced functional networks is characterized by the allegiance matrix to give a general picture of the functional roles of brain regions and systems across states. This technique was first introduced to characterize how brain regions were coordinated during learning [40], and then to characterize the functional properties of cognitive subsystems [5]. We observed functional clustering not directly explained by underlying structure, indicating regional dynamics can modulate structure-function relations. Previous computational works have examined brain dynamics either globally [21] or at the node level [46]. However, brain regions are known to be activated cohesively along the so-called cognitive subnetworks for healthy functioning [6,47]. We found that cognitive synchronization patterns are more sensitive to which structural region is stimulated, suggesting cognitive synchronization may encode task specificity. Theoretical work has also agreed with this by showing cognitive synchronization patterns are sensitive to the stimulated system [27], while their mathematical model is not constrained by realistic functional data. We extend their work by finding cognitive metastability is relatively consistent across task-relevant states and exhibiting opposite directions of changes between stimulation schemes. Our results, to some extent, demonstrate the potential of whole-brain dynamical models to integrate stimuli in a functionally meaningful way, and the potential to extend the analysis framework to multiple brain states, such as during cognitive progressions.

Second, we found cognitive metastable networks as a potential dynamical maker associated with task-relevant brain activities. Cognitive metastability exhibits a relatively consistent network architecture across states, suggesting it may encode a more task-general property during cognitive processing, an inherent property conferred by brain organization. We also demonstrate that the functional role of cognitive systems is embodied in this network structure, reflecting a broad classification between cognitive control systems and sensory systems and agreeing with their realistic system function (Fig. 7). Empirical evidence suggests that the attentional system shows greater variability in functional roles than the default mode, visual, and somatosensory systems across tasks [5], and also between subjects [45]. This result demonstrates a link between phase dynamics at the system level and functionally meaningful neural communication during cognitive processing.

Metastability, indicating the temporal fluctuations of phase interactions, is an assumed mechanism of functional segregation and integration which is associated with cognitive performance [11,48]. Theoretical works have revealed that the emerging spatiotemporal patterns of brain dynamics resemble the empirical human resting-state network best when the model operates in the metastable regime [12,15,25]. Empirical evidence has linked metastability with cognitive performance in various contexts, with reduced metastability in Parkinson’s disease [8] and senescence [18], and increased under tasks [17]. Thereby it is speculated that a higher level of metastability is linked to higher cognitive performance, while a lower level of metastability will result in impaired

cognitive performance [18]. In our simulations, positive and negative stimulation schemes lead to dynamics changing in the opposite direction at global and systems levels (Figs. 6 and 7), with patterns observed in empirical data resembling those in positive schemes. If positive schemes are related to normal cognitive processing, then negative schemes may be associated with a very different condition such as cognitive impairment [8,17,18,44,49]. A great advantage of investigating phase relationships between brain signals is that it allows a direct comparison between theoretical and empirical results. We use rest and seven-task fMRI data from HCP to provide evidence for the general network architecture in cognitive metastability across states and its association with system function. Our results are also partially supported by a recent empirical work leveraging human functional data from multiple task paradigms to inspect spontaneous synchronization and metastability couplings among cognitive subnetworks [17]. These findings accord with us in the following aspects. First, task general states are characterized by higher metastability in cognitive control systems and lower metastability in sensory and processing systems [Figs. 7(a) and 8(a)]. Second, the specificity of each task is better captured by the synchronization patterns than metastability [Figs. 6(a) and 6(b)]. Reproduction of the finding with a bottom-up model can strongly support the genuineness of such observations to be an intrinsic property of the brain system.

Our paper serves as a proof-of-concept study with apparent limitations. The model construction was based on a

coarse-grained parcellation cortex which limits the interpretability of system function at a low spatial resolution. Finer parcellations will be used in future work to obtain a better correspondence between empirical and theoretical results. We also performed a relatively simple stimulation protocol in the *in silico* experiments. The stimulation protocol could be designed based on known mappings of cognitive processing to brain regions, for example, the language task-specific circuit [26], depending on the problem to be solved at hand. Another apparent drawback is the poor representation of cross-hemispheres connections in the model's SC matrix  $C$ , which is an inherent limitation rooted in diffusion tensor imaging techniques. This would lead to an inevitable low quality in the simulations. Finally, the presented results are derived on a group basis, while individual interpretability is of crucial importance in brain engineering for the ultimate goal of personalized medical interventions [26,45]. We attempt to bridge this gap in future works by incorporating personalized structural and functional imaging data into whole-brain network modeling, with the purpose of establishing a model-based link between individual structure, brain dynamics, and cognition.

#### ACKNOWLEDGMENTS

This research was supported by the National Natural Science Foundation of China (Grants No. 11932003, No. 12332004, No. 12272092, and No. 11972115).

- 
- [1] H.-J. Park and K. Friston, *Science* **342**, 1238411 (2013).
  - [2] Z. Dai and Y. He, *Neuroscience Bulletin* **30**, 217 (2014).
  - [3] M. D. Fox and M. E. Raichle, *Nat. Rev. Neurosci.* **8**, 700 (2007).
  - [4] M. W. Cole, D. S. Bassett, J. D. Power, T. S. Braver, and S. E. Petersen, *Neuron* **83**, 238 (2014).
  - [5] M. G. Mattar, M. W. Cole, S. L. Thompson-Schill, and D. S. Bassett, *PLoS Comput. Biol.* **11**, e1004533 (2015).
  - [6] M. A. Bertolero, B. T. T. Yeo, and M. D'Esposito, *Proc. Natl. Acad. Sci. USA* **112**, E6798 (2015).
  - [7] F. Hancock, F. Rosas, P. Mediano, A. Luppi, J. Cabral, O. Dipasquale, and F. Turkheim, *J. R. Soc. Interface.* **19**, 20220214 (2022).
  - [8] L. Wang, C. Zhou, W. Cheng, E. T. Rolls, P. Huang, N. Ma, Y. Liu, Y. Zhang, X. Guan, T. Guo, J. Wu, T. Gao, M. Xuan, Q. Gu, X. Xu, B. Zhang, W. Gong, J. Du, W. Zhang, J. Feng *et al.*, *Human Brain Mapping* **43**, 1598 (2022).
  - [9] P. Fries, *Neuron* **88**, 220 (2015).
  - [10] M. Shanahan, *Chaos* **20**, 013108 (2010).
  - [11] E. Tognoli and J. A. S. Kelso, *Neuron* **81**, 35 (2014).
  - [12] J. Cabral, H. Luckhoo, M. Woolrich, M. Joansson, H. Mohseni, A. Baker, M. L. Kringelbach, and G. Deco, *NeuroImage* **90**, 423 (2014).
  - [13] G. Deco and M. L. Kringelbach, *Trends Neurosci.* **39**, 125 (2016).
  - [14] Y. Kuramoto, in *Chemical Oscillations, Waves, and Turbulence*, edited by H. Haken, Springer Series in Synergetics Vol. 19 (Springer-Verlag, Berlin, 1984).
  - [15] A. Ponce-Alvarez, G. Deco, P. Hagmann, G. L. Romani, D. Mantini, and M. Corbetta, *PLoS Comput. Biol.* **11**, e1004100 (2015).
  - [16] B. M. Jobst, R. Hindriks, H. Laufs, E. Tagliazucchi, G. Hahn, A. Ponce-Alvarez, A. B. A. Stevner, M. L. Kringelbach, and G. Deco, *Sci. Rep.* **7**, 4634 (2017).
  - [17] T. H. Alderson, A. L. W. Bokde, J. A. S. Kelso, L. Maguire, and D. Coyle, *Hum. Brain Mapp.* **41**, 3212 (2020).
  - [18] S. Naik, A. Banerjee, R. S. Bapi, G. Deco, and D. Roy, *Trends Cogn. Sci.* **21**, 509 (2017).
  - [19] D. Keeser, T. Meindl, J. Bor, U. Palm, O. Pogarell, C. Mulert, J. Brunelin, H.-J. Möller, M. Reiser, and F. Padberg, *J. Neurosci.* **31**, 15284 (2011).
  - [20] U. Amadi, A. Ilie, H. Johansen-Berg, and C. J. Stagg, *NeuroImage* **88**, 155 (2014).
  - [21] S. F. Muldoon, F. Pasqualetti, S. Gu, M. Cieslak, S. T. Grafton, J. M. Vettel, and D. S. Bassett, *PLoS Comput. Biol.* **12**, e1005076 (2016).
  - [22] C. J. Honey, O. Sporns, L. Cammoun, X. Gigandet, J. P. Thiran, R. Meuli, and P. Hagmann, *Proc. Natl. Acad. Sci. USA* **106**, 2035 (2009).
  - [23] G. Deco, A. R. McIntosh, K. Shen, R. M. Hutchison, R. S. Menon, S. Everling, P. Hagmann, and V. K. Jirsa, *J. Neurosci.* **34**, 7910 (2014).
  - [24] E. C. A. Hansen, D. Battaglia, A. Spiegler, G. Deco, and V. K. Jirsa, *NeuroImage* **105**, 525 (2015).
  - [25] G. Deco, M. L. Kringelbach, V. K. Jirsa, and P. Ritter, *Sci. Rep.* **7**, 3095 (2017).

- [26] K. Bansal, J. D. Medaglia, D. S. Bassett, J. M. Vettel, and S. F. Muldoon, *PLoS Comput. Biol.* **14**, e1006487 (2018).
- [27] K. Bansal, J. O. Garcia, S. H. Tompson, T. Verstynen, J. M. Vettel, and S. F. Muldoon, *Sci. Adv.* **5**, eaau8535 (2019).
- [28] D. C. Van Essen, S. M. Smith, D. M. Barch, T. E. Behrens, E. Yacoub, and K. Ugurbil, *NeuroImage* **80**, 62 (2013).
- [29] M. F. Glasser, S. N. Sotiropoulos, J. A. Wilson, T. S. Coalson, B. Fischl, J. L. Andersson, J. Xu, S. Jbabdi, M. Webster, J. R. Polimeni, D. C. Van Essen, and M. Jenkinson, *NeuroImage* **80**, 105 (2013).
- [30] R. S. Desikan, F. Ségonne, B. Fischl, B. T. Quinn, B. C. Dickerson, D. Blacker, R. L. Buckner, A. M. Dale, R. P. Maguire, B. T. Hyman, M. S. Albert, and R. J. Killiany, *NeuroImage* **31**, 968 (2006).
- [31] P. Wang, R. Kong, X. Kong, R. Liégeois, C. Orban, G. Deco, M. P. van den Heuvel, and B. Thomas Yeo, *Sci. Adv.* **5**, eaat7854 (2019).
- [32] G. Deco, A. Ponce-Alvarez, D. Mantini, G. L. Romani, P. Hagmann, and M. Corbetta, *J. Neurosci.* **33**, 11239 (2013).
- [33] G. Deco, J. Cabral, M. W. Woolrich, A. B. Stevner, T. J. van Hartevelt, and M. L. Kringelbach, *NeuroImage* **152**, 538 (2017).
- [34] F. Freyer, J. A. Roberts, P. Ritter, and M. Breakspear, *PLoS Comput. Biol.* **8**, e1002634 (2012).
- [35] M. L. Kringelbach, A. R. McIntosh, P. Ritter, V. K. Jirsa, and G. Deco, *Trends Cogn. Sci.* **19**, 616 (2015).
- [36] G. Deco, V. K. Jirsa, and A. R. McIntosh, *Nat. Rev. Neurosci.* **12**, 43 (2011).
- [37] P. Donnelly-Kehoe, V. M. Saenger, N. Lisofsky, S. Kühn, M. L. Kringelbach, J. Schwarzbach, U. Lindenberger, and G. Deco, *Hum. Brain Mapp.* **40**, 2967 (2019).
- [38] V. D. Blondel, J.-L. Guillaume, R. Lambiotte, and E. Lefebvre, *J. Stat. Mech.: Theory Exp.* (2008) P10008.
- [39] M. A. Riolo and M. E. J. Newman, *Phys. Rev. E* **101**, 052306 (2020).
- [40] D. S. Bassett, M. Yang, N. F. Wymbs, and S. T. Grafton, *Nat. Neurosci.* **18**, 744 (2015).
- [41] G. Deco, J. Cabral, V. M. Saenger, M. Boly, E. Tagliazucchi, H. Laufs, E. Van Someren, B. Jobst, A. Stevner, and M. L. Kringelbach, *NeuroImage* **169**, 46 (2018).
- [42] X. Di, S. Gohel, E. Kim, and B. Biswal, *Front. Hum. Neurosci.* **7**, 493 (2013).
- [43] A. Córdova-Palomera, T. Kaufmann, K. Persson, D. Alnæs, N. T. Doan, T. Moberget, M. J. Lund, M. L. Barca, A. Engvig, A. Brækhus, K. Engedal, O. A. Andreassen, G. Selbæk, and L. T. Westlye, *Sci. Rep.* **7**, 40268 (2017).
- [44] T. H. Alderson, A. L. Bokde, J. S. Kelso, L. Maguire, and D. Coyle, *NeuroImage* **183**, 438 (2018).
- [45] C. Gratton, T. O. Laumann, A. N. Nielsen, D. J. Greene, E. M. Gordon, A. W. Gilmore, S. M. Nelson, R. S. Coalson, A. Z. Snyder, B. L. Schlaggar, N. U. Dosenbach, and S. E. Petersen, *Neuron* **98**, 439 (2018).
- [46] F. Váša, M. Shanahan, P. J. Hellyer, G. Scott, J. Cabral, and R. Leech, *NeuroImage* **118**, 456 (2015).
- [47] J. M. Shine, P. G. Bissett, P. T. Bell, O. Koyejo, J. H. Balsters, K. J. Gorgolewski, C. A. Moodie, and R. A. Poldrack, *Neuron* **92**, 544 (2016).
- [48] R. Wang, M. Liu, X. Cheng, Y. Wu, A. Hildebrandt, and C. Zhou, *Proc. Natl. Acad. Sci. USA* **118**, e2022288118 (2021).
- [49] P. J. Hellyer, G. Scott, M. Shanahan, D. J. Sharp, and R. Leech, *J. Neurosci.* **35**, 9050 (2015).